

Cite this: *Chem. Sci.*, 2025, 16, 2373

All publication charges for this article have been paid for by the Royal Society of Chemistry

Symmetrical and asymmetrical surface structure expansions of silver nanoclusters with atomic precision†

Honglei Shen,[‡]^a Pu Wang,[‡]^b Jiawei Xu,^a Ziwei Fu,^a Xi Kang,[‡]^a Yong Pei^{*b} and Manzhou Zhu[‡]^a

Controlling symmetrical or asymmetrical growth has allowed a series of novel nanomaterials with prominent physicochemical properties to be produced. However, precise and continuous size growth based on a preserved template has long been a challenging pursuit, yet little has been achieved in terms of manipulation at the atomic level. Here, a correlated silver cluster series has been established, enabling atomically precise manipulation of symmetrical and asymmetrical surface structure expansions of metal nanoclusters. Specifically, the C_3 -axisymmetric $Ag_{29}(BDTA)_{12}(PPh_3)_4$ nanocluster underwent symmetrical and asymmetrical surface structure expansions *via* an acid-mediated synthetic procedure, giving rise to C_3 -axisymmetric $Ag_{32}(BDTA)_{12}(PPh_3)_{10}$ and C_1 -axisymmetric $Ag_{33}(BDTA)_{12}(PPh_3)_{11}$, respectively. In addition, structural transformations, including structural degradation from Ag_{32} to Ag_{29} and asymmetrical structural expansion from Ag_{32} to Ag_{33} , were rationalized theoretically. More importantly, the asymmetrically structured Ag_{33} nanoclusters followed a chiral crystallization mode, and their crystals displayed high optical activity, derived from CD and CPL characterization. This work not only provides an important model for unlocking the symmetrical/asymmetrical size growth mechanism at the atomic level but also pioneers a promising approach to activate the optical activity of cluster-based nanomaterials.

Received 9th October 2024
Accepted 2nd January 2025

DOI: 10.1039/d4sc06847e

rsc.li/chemical-science

Introduction

The surface structure expansion of nanomaterials has emerged as a versatile approach to control their morphologies, increase their structural complexity, and enhance their functionalities for downstream applications.^{1,2} According to the different growth orientations, the surface structure expansion follows symmetrical or asymmetrical growth patterns, laying the foundation for constructing isotropic or anisotropic nanomaterials, respectively.³ While most work on controlling nanomaterial morphology revolves around symmetrical growth, the introduction of asymmetrical factors and thus symmetry breaking

has also emerged as a powerful route to enrich nanomaterials with new shapes and complex morphologies as well as unprecedented functionalities.^{3,4} To date, a variety of symmetry-preserved or symmetry-broken nanocrystals have been reported, together with some insights into their symmetrical or asymmetrical growth mechanisms;^{5–8} however, most of these mechanisms have been elucidated on the basis of microscopy, and little has been achieved in terms of understanding at the atomic level. The in-depth comprehension of the symmetrical/asymmetrical structure expansion and atomically precise control over growth orientations require precise molecular entities to serve as model nanosystems and accurate molecular tools.

Metal nanoclusters are among the most promising nanomaterials for investigating structural evolutions owing to their uniform sizes and precise structures.^{9–15} Besides, the prominent quantum size effects and discrete electronic energy levels enable cluster-based nanomaterials with structure-dependent physicochemical properties, and the structure–property correlations are accessible at the atomic level.^{16–28} Several efficient strategies have been exploited to regulate the structures of metal nanoclusters, such as ligand engineering, kernel alloying, counterion regulation, intercluster reactions, *etc.*, involving both the molecular and supramolecular chemistry of these programmable nanomaterials.^{29–36} Based on these strategies, several cluster cases of surface structure expansion (or size

^aDepartment of Chemistry, Centre for Atomic Engineering of Advanced Materials, Key Laboratory of Structure and Functional Regulation of Hybrid Materials of Ministry of Education, Institutes of Physical Science and Information Technology, Anhui Province Key Laboratory of Chemistry for Inorganic/Organic Hybrid Functionalized Materials, Anhui University, Hefei, Anhui 230601, China. E-mail: kangxi_chem@ahu.edu.cn; zmmz@ahu.edu.cn

^bDepartment of Chemistry, Key Laboratory of Environmentally Friendly Chemistry and Applications of Ministry of Education, Xiangtan University, Xiangtan, Hunan 411105, P. R. China. E-mail: ypei2@xtu.edu.cn

† Electronic supplementary information (ESI) available: Scheme S1, Fig. S1–S20 and Tables S1–S5. CCDC 2243513, 2243517, 2243519 and 2243542. For ESI and crystallographic data in CIF or other electronic format see DOI: <https://doi.org/10.1039/d4sc06847e>

‡ H. S. and P. W. contributed equally to this work.



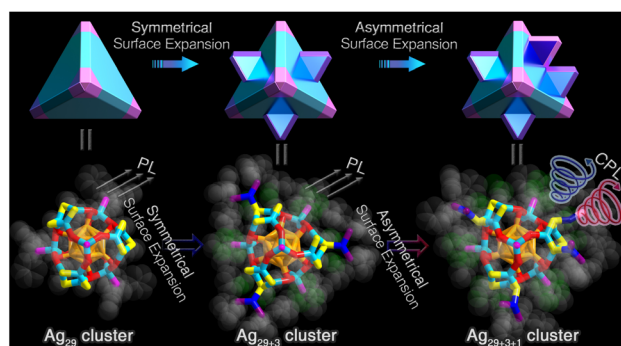
growth) have been reported, while most of these structural manipulations were non-directional and discontinuous.^{37–43} In addition, the success of controlling the symmetrical/asymmetrical structure expansion of clusters critically relies on the ability to retain/lift the confinement on symmetry by the underlying surface units of the molecular structures; however, achieving this control has long been a challenging pursuit. The attainment of controlled symmetrical or asymmetrical size growth of metal clusters with preserved frameworks is highly desirable for revealing the structural growth mechanism and the corresponding structure–property correlations at the atomic level.

Herein, the continuous size growth, involving both symmetrical and asymmetrical surface structure expansions, has been accomplished for metal nanoclusters with a preserved framework. The acid-mediated preparation in the one-pot silver-cluster synthetic procedure directed the generation of three correlated Ag nanoclusters (Schemes 1 and S1†): (i) the $\text{Ag}_{29}(\text{BDTA})_{12}(\text{PPh}_3)_4$ nanocluster (Ag_{29} for short, where BDTA represents 3,5-dithiolbenzoic acid) with C_3 axial symmetry, (ii) the C_3 -axisymmetric $\text{Ag}_{32}(\text{BDTA})_{12}(\text{PPh}_3)_{10}$ nanocluster (Ag_{32} for short) exhibiting symmetrical surface structure expansion relative to Ag_{29} , and (iii) the C_1 -axisymmetric $\text{Ag}_{33}(\text{BDTA})_{12}(\text{PPh}_3)_{11}$ nanocluster (Ag_{33} for short) displaying asymmetrical surface structure expansion relative to Ag_{29} and Ag_{32} . The

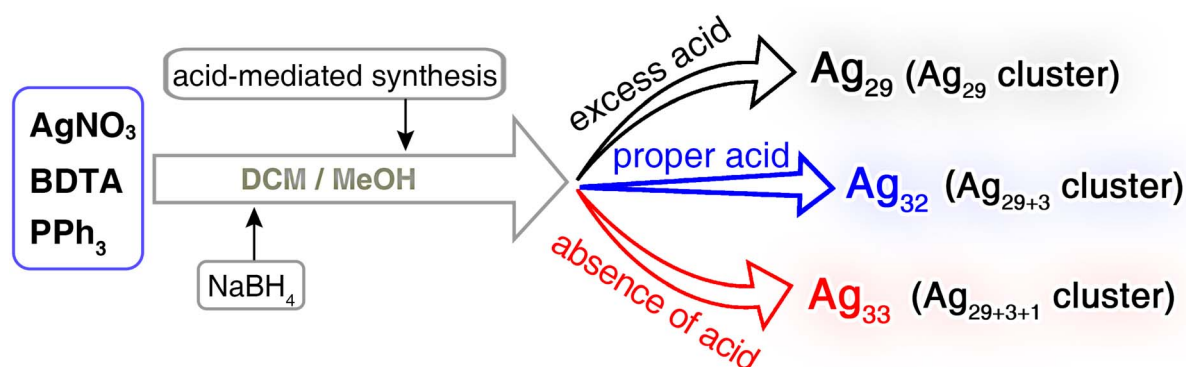
continuous structural transformations were rationalized *via ab initio* calculations, including the structural degradation from Ag_{32} to Ag_{29} and the asymmetrical structural expansion from Ag_{32} to Ag_{33} . Significantly, the structurally asymmetrical Ag_{33} nanocluster followed a chiral crystallization mode, and its crystals displayed high optical activity, derived from circular dichroism (CD) and circularly polarized luminescence (CPL) characterization. In vivid contrast, the structurally symmetrical Ag_{29} and Ag_{32} nanoclusters were racemic in the crystal state, encompassing equal amounts of *S*- and *R*-cluster enantiomers in the crystal lattice. Overall, the findings in this work provide impetus for future experimental and theoretical developments in the symmetrical growth or symmetry breaking of metal nanoclusters.

Results and discussion

The Ag_{29} , Ag_{32} , and Ag_{33} nanoclusters were prepared *via* a one-pot acid-mediated synthetic procedure (Scheme 2; see the ESI† for more details). Specifically, after the reduction of NaBH_4 , the introduction of different amounts of HCl directed the generation of structure-correlated silver nanoclusters, Ag_{29} , Ag_{32} , or Ag_{33} with an analogous molecular framework but different surface environments (Tables S1–S4†). Of note, previous studies have demonstrated the pH-dependent formation of metal nanoclusters, demonstrating the importance of an acid–base environment for nanocluster regulation.^{44,45} For the cluster homologue of Ag_{29} , the $\text{Ag}_{29}(\text{BDT})_{12}(\text{PPh}_3)_4$ nanocluster (Ag_{29} -BDT for short; BDT = 1,3-benzene dithiol) might be unstable in the presence of acid, and we observed that the introduction of HCl inhibited the nanocluster preparation. By comparison, for the BDTA-stabilized silver clusters in this work, due to the existence of carboxyl groups on thiol ligands, the acid sensitivity of BDTA was transmitted to the cluster framework, which provided us an opportunity to precisely control the cluster structures by regulating the amount of HCl among the synthesis.⁴⁶ In addition, the BDTA-stabilized Ag_{29} and Ag_{29} -BDT presented the same cluster framework, demonstrating that the introduction of carboxyl functional groups would not significantly change the coordination ability (or the nucleophilicity) of the bidentate thiol ligand. The successful structure



Scheme 1 Schematic illustration of the symmetrical surface expansion from Ag_{29} to Ag_{32} nanoclusters and the asymmetrical surface expansion from Ag_{32} to Ag_{33} nanoclusters.



Scheme 2 Schematic illustration of the synthetic procedure for Ag_{29} , Ag_{32} , and Ag_{33} nanoclusters *via* an acid-mediated synthetic procedure.



determination of this silver cluster series (*i.e.*, Ag_{29} , Ag_{32} , and Ag_{33}) enabled the downstream mechanism elucidation towards the symmetrical and asymmetrical surface structure expansions of metal clusters with atomic precision.

The geometric structure of Ag_{29} was the same as that of Ag_{29} -BDT reported previously,⁴⁷ except for their different peripheral bidentate thiol ligands (Fig. S1†). Structurally, the Ag_{29} nanocluster contained an icosahedral Ag_{13} kernel that was stabilized from four $\text{Ag}_3(\text{SR}')_6$ units *via* sharing the bidentate BDTA thiol ligands, where SR' was half of the BDTA ligand (Fig. 1A–C). Then, the obtained $\text{Ag}_{25}(\text{BDTA})_{12}$ framework was capped by four vertex $\text{Ag}-\text{PPh}_3$ units to construct the overall structure of Ag_{29} -BDT (Fig. 1D and E). The Ag_{29} exhibited a highly symmetrical overall structure with four C_3 symmetry axes, passing through the vertex $\text{Ag}-\text{PPh}_3$ unit and the innermost Ag kernel (Fig. 1F).

The total structure of the Ag_{32} nanocluster represented the symmetrical surface structure expansion relative to the Ag_{29} cluster framework (Fig. S2†). Specifically, three terminal $\text{Ag}_1(\text{PPh}_3)_2$ units were symmetrically arranged onto the Ag_{29} framework by anchoring to the $\text{Ag}_3(\text{SR}')_3$ ring, resulting in the overall structure of $\text{Ag}_{32}(\text{BDTA})_{12}(\text{PPh}_3)_{10}$ (Fig. 1G–I). Although the complete structure of Ag_{32} still followed C_3 symmetry (Fig. S2†), symmetry degradation was discovered in contrast to the Ag_{29} nanocluster. Indeed, due to the introduction of three symmetric $\text{Ag}_1(\text{PPh}_3)_2$ units on its surface, the Ag_{32} nanocluster only showed one C_3 symmetry axis that crossed the innermost Ag kernel and a vertex $\text{Ag}-\text{PPh}_3$ unit.

Continuous size growth from Ag_{32} gave rise to the generation of the Ag_{33} nanocluster, which exhibited asymmetrical surface structure expansion relative to the Ag_{32} cluster framework (Fig. S3†). As shown in Fig. 1J–L, an extra $\text{Ag}_1(\text{PPh}_3)_1$ surface unit connected with an inward S atom of the $\text{Ag}_{32}(\text{BDTA})_{12}(\text{PPh}_3)_{10}$ structure to form the overall structure of Ag_{33} . In the meantime, the coordination sites of the three terminal $\text{Ag}_1(\text{PPh}_3)_2$ units on the cluster surface altered to an uneven distribution (Fig. S3†). The combination of two asymmetric factors, *i.e.*, the uneven distributions of (i) $\text{Ag}_1(\text{PPh}_3)_1$ and (ii) $\text{Ag}_1(\text{PPh}_3)_2$, contributed to the symmetry breaking of the Ag_{33} nanocluster, making Ag_{33} asymmetrical with C_1 symmetry (Fig. 1L). Collectively, from the aspect of structural evolution, the $\text{Ag}_{32}/\text{Ag}_{33}$ nanoclusters could be viewed as the size-growth products of the Ag_{29} cluster precursor through symmetrical/asymmetrical surface structure expanding patterns. Besides, the Ag_{32} and Ag_{33} nanoclusters maintained the original Ag_{29} structure in terms of their consistent Ag_{29} -containing frameworks and analogous bond lengths. Fig. S4† compares the average lengths of the $\text{Ag}(\text{icosahedral surface})-\text{Ag}(\text{icosahedral surface})$, $\text{Ag}(\text{icosahedral surface})-\text{S}(\text{shell})$, $\text{Ag}(\text{shell})-\text{S}(\text{shell})$, and $\text{Ag}(\text{vertex})-\text{P}(\text{vertex})$ bonds in Ag_{29} -BDT, Ag_{29} , Ag_{32} , and $R/S\text{-Ag}_{33}$ nanoclusters. The differences in the corresponding bond lengths were all less than 1%, demonstrating the structural integrity of the Ag_{29} framework among the symmetrical/asymmetrical surface structure expanding processes. In addition, the carboxylated surface endowed the Ag_{29} nanocluster with an acid-resistant

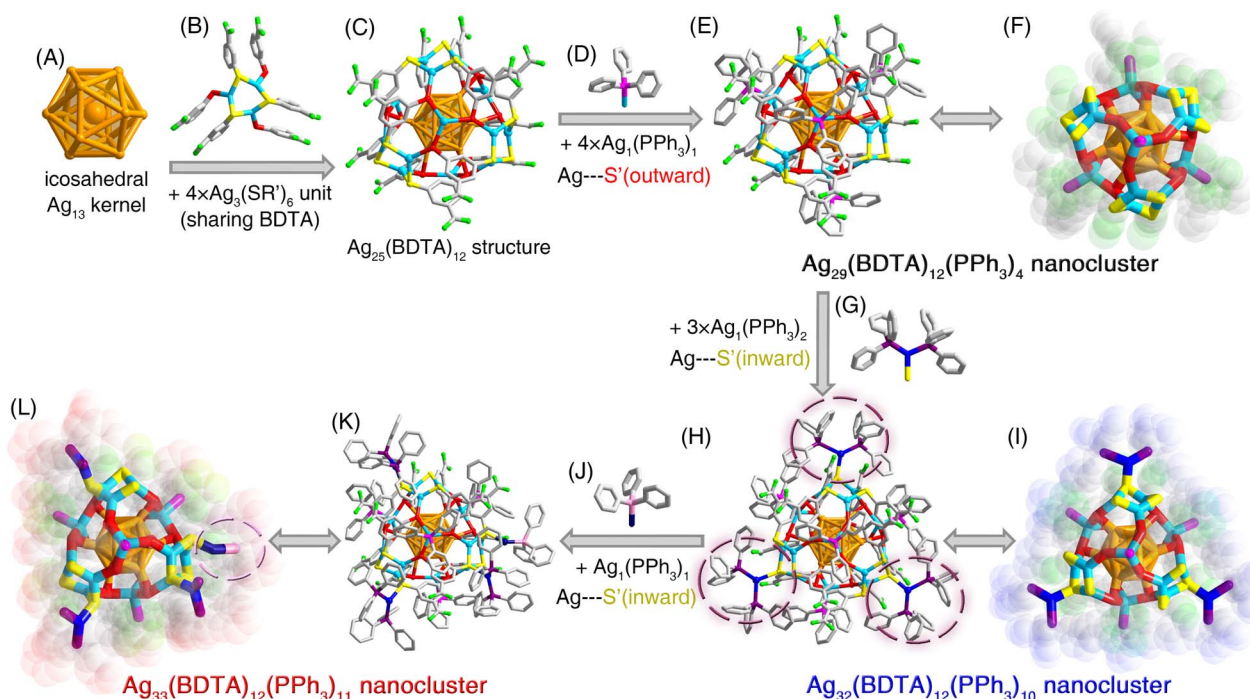


Fig. 1 Structural anatomy of Ag_{29} , Ag_{32} , and Ag_{33} nanoclusters. (A) The icosahedral Ag_{13} kernel. (B) The $\text{Ag}_{12}(\text{BDTA})_{12}$ surface structure contains four $\text{Ag}_3(\text{SR}')_6$ surface units *via* sharing the bidentate BDTA thiol ligands. (C) The $\text{Ag}_{25}(\text{BDTA})_{12}$ structure. (D) The four $\text{Ag}_1(\text{PPh}_3)_1$ vertex units. (E and F) The overall structure of the $\text{Ag}_{29}(\text{BDTA})_{12}(\text{PPh}_3)_4$ nanocluster. (G) The three $\text{Ag}_1(\text{PPh}_3)_2$ surface symmetrical expanding units. (H and I) The overall structure of the $\text{Ag}_{32}(\text{BDTA})_{12}(\text{PPh}_3)_{10}$ nanocluster. (J) The $\text{Ag}_1(\text{PPh}_3)_1$ surface asymmetrical expanding unit. (K and L) The overall structure of the $\text{Ag}_{33}(\text{BDTA})_{12}(\text{PPh}_3)_{11}$ nanocluster. Color legends: orange/light blue/blue spheres, Ag ; red/yellow spheres, S ; magenta/purple/pink spheres, P ; green sphere, O ; grey sphere, C . All H atoms are omitted for clarity.



characteristic, and Ag₂₉ showed enhanced stability relative to Ag₂₉-BDT in an acidic environment (Fig. S5†).

Electrospray ionization mass spectrometry (ESI-MS) of the Ag₂₉ nanocluster showed an intense signal at 1779.56 Da in negative mode with characteristic isotopic peaks separated by a *m/z* of 0.33 Da, corresponding to the chemical formula of [Ag₂₉(BDTA)₁₂]³⁻ (Fig. S6†). In this context, the vertex PPh₃ ligands of Ag₂₉ were dissociated entirely because of the high collision energy during the mass detection. The Ag₂₉ nanocluster presented a closed-shell electronic structure with a nominal electron count of eight (*i.e.*, 29(Ag) – 12 × 2(SR) + 3(charge) = 8), consistent with the icosahedral unit in the cluster framework.⁴⁸ Given the structural consistency among these structure-correlated silver nanoclusters, the Ag₃₂ and Ag₃₃ nanoclusters should manifest the same nominal electron counts as eight. Consequently, the Ag₃₂ cluster molecule would be electrically neutral, while the Ag₃₃ cluster molecule would carry a “+1” charge. However, we failed to observe the characteristic mass signals of the two surface-expanded nanoclusters in ESI-MS (Fig. S7†). In addition, ³¹P NMR (Nuclear Magnetic Resonance) and elemental analyses were performed to verify the purity and demonstrate the symmetry of such nanoclusters (Fig. S8 and Table S5†).

The structural-property correlations of these structure-correlated silver nanoclusters were investigated. Fig. 2A compares the optical absorptions spectra of the four

nanoclusters in the solution state. The DMF solutions of all nanoclusters, including Ag₂₉-BDT, Ag₂₉, Ag₃₂, and Ag₃₃, exhibited almost the same optical absorption spectra with an intense peak at 440 nm and several shoulder bands at 320, 364, and 515 nm (Fig. 2A). Indeed, although Ag₂₉, Ag₃₂, and Ag₃₃ nanoclusters exhibited comparable surface structures, their intrinsic kernel structures were identical as Ag₂₉(BDTA)₁₂(PPh₃)₄. Such similar absorption spectra demonstrated that the electronic orbits of these silver nanoclusters were primarily constituted by the innermost Ag₂₉ framework, while they were less relevant to the surface Ag-PPh₃ stabilizers. The photoluminescence (PL) of Ag₂₉-BDT, Ag₂₉, Ag₃₂, and Ag₃₃ nanoclusters was then measured in the solution state. The normalized PL spectra suggested that both Ag₂₉-BDT and Ag₂₉ emitted at 672 nm; by comparison, the emission of Ag₃₂ red-shifted to 682 nm, while that of Ag₃₃ blue-shifted to 662 nm (Fig. 2B, inset). Under 440 nm excitation, the three BDTA-stabilized nanoclusters showed remarkable PL enhancement relative to Ag₂₉-BDT. Specifically, the Ag₃₂ nanocluster showed a ~27-fold enhancement in emission intensity compared to Ag₂₉-BDT (Fig. 2B and C), and the PL intensity sequence was Ag₃₂ (PL QY of 25.5%) > Ag₂₉ (PL QY of 5.8%) > Ag₃₃ (PL QY of 3.8%) > Ag₂₉-BDT (PL QY of 0.9%).

The significant PL enhancement of BDTA-stabilized nanoclusters might originate from their intramolecular C–H···π and π···π···π interactions (Fig. S9†), which remarkably restrained the vibrations/rotations of cluster molecules.⁴⁶ Besides, the

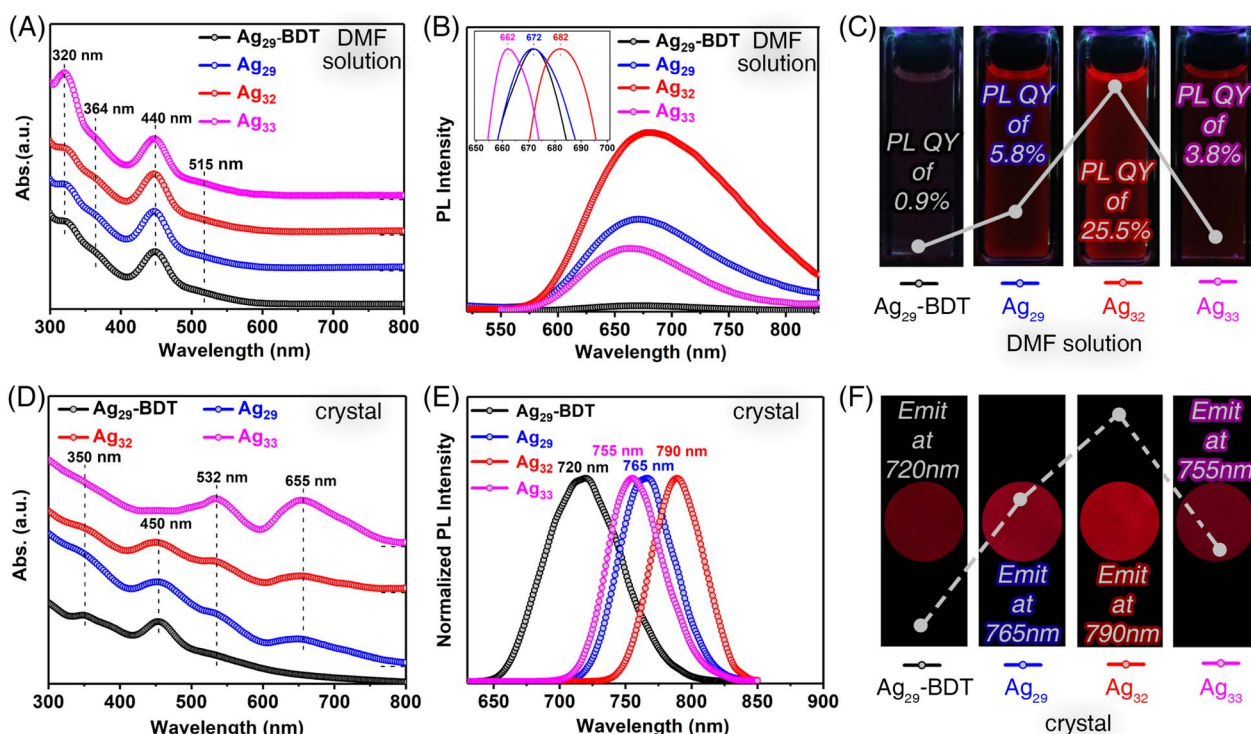


Fig. 2 Optical properties of Ag₂₉-BDT, Ag₂₉, Ag₃₂, and Ag₃₃ nanoclusters. (A) Optical absorption spectra of the four nanoclusters in their DMF solutions. (B) Photoluminescence emissions of the four nanoclusters in their DMF solutions. Inset: comparison of the normalized emission wavelengths. (C) Photos of the photoluminescence of the four nanoclusters in DMF. Inset line: changing trends of the PL QY. (D) Optical absorption spectra of the four nanocluster crystals. (E) Normalized photoluminescence emissions of the four nanoclusters in their crystals. (F) Photos of the photoluminescence of the four nanocluster crystals. Inset line: changing trends of the emission wavelength.



introduced Ag-PPh₃ surface units in Ag₃₂ and Ag₃₃ further restrained the molecular vibrations/rotations. Accordingly, the energy dissipation of the photo-excited clusters through the radiative transition increased, accounting for the emission enhancement of the BDTA-stabilized silver nanoclusters. Of note, the Ag₃₃ nanocluster with asymmetrical surface structures might exhibit additional intracluster vibrations from the Ag₁(PPh₃)₁ surface asymmetrical expanding unit, resulting in attenuated PL intensity relative to the Ag₃₂ nanocluster. In addition, due to the different intracluster interactions, the energy dissipation pathway of these excited cluster molecules might be affected, and thus their emission wavelengths were slightly different.

The single crystal-based crystals of the four structure-correlated silver nanoclusters exhibited more apparent differences in optical properties (see the ESI† for more details on the preparation of such crystals). The crystals of Ag₂₉-BDT displayed comparable optical absorption spectra to its DMF solution. However, for the three BDTA-stabilized silver nanoclusters, absorption peaks at 532 and 655 nm were observed for their crystals (Fig. 2D), which were optically salient in the corresponding DMF solutions. Besides, the crystals of Ag₂₉-BDT showed an intense emission at 720 nm, while obvious red-shifts were detected for the emissions of BDTA-stabilized nanoclusters (Fig. 2E). In particular, the brightest Ag₃₂ cluster crystals emitted at 790 nm, representing a 70 nm red-shift relative to Ag₂₉-BDT (Fig. 2F). The conspicuous differences in optical absorption (*i.e.*, 655 nm) and emissions of these structure-correlated silver nanoclusters in different forms (crystal and solution) arose from their distinct combinations of the electronic coupling and the lattice-origin, non-radiative decay

pathways occurring through electron–phonon interactions.^{49–51} Indeed, in the solution state, these nanoclusters are more like independent individuals, which are uniformly dispersed in the system. When the cluster molecules spontaneously crystallize, they are fixed within the crystal lattice with intermolecular interactions. This partially affects the electronic structure of the clusters, which in turn influences the photophysical properties of nanoclusters. Besides, the presence of rich carboxyl functional groups might trigger such electron–phonon interactions in cluster crystalline lattices. In addition, these differences between the surface inactive Ag₂₉-BDT and surface-carboxylated Ag₂₉, Ag₃₂, and Ag₃₃ could also be explained in terms of their diverse surface chemistry as well as intra-/inter-molecular interactions.⁵²

Theoretical efforts were made to rationalize the structural transformations among these structure-correlated silver nanoclusters. Considering that the Ag₃₂ nanocluster underwent symmetrical structural degradation to generate Ag₂₉ in an acidic environment (Fig. S10†), we theoretically investigated the corresponding structural transformation mechanism. Here, we simulated the detachment mechanism of an Ag(PPh₃)₂ group from the Ag₃₂ nanocluster as an example to reveal the structural degradation process. As shown in Fig. 3A and S11,† the H proton reacted with the S site of the Ag₃(SR')₃ ring to form the most stable Ag₃₂P₁₀H–C intermediate (marked as Path 3), and the reaction energy was –10.44 eV. This process was beneficial to weaken the interaction between the Ag(PPh₃)₂ group and the surface Ag₃(SR')₃ ring, resulting in an increase of the Ag–S bond length from 2.51 to 2.63 Å. Although another two processes could also effectively weaken the Ag–S bond when the H proton attacked the surface Ag site (marked as Path 1 and Path 2;

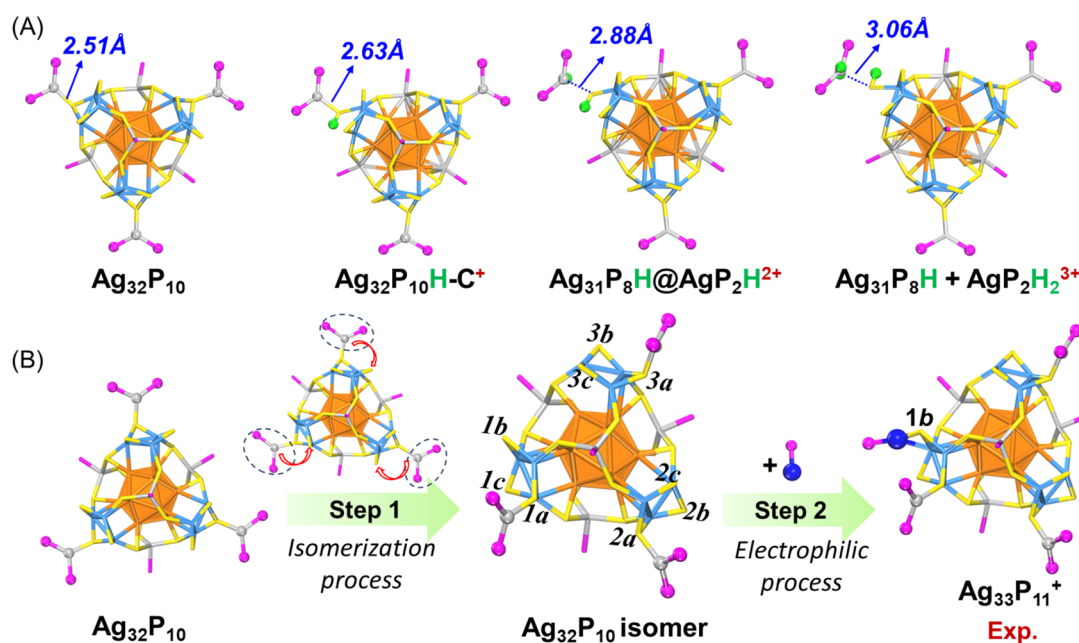


Fig. 3 Theoretical investigation of the corresponding cluster structural transformations. (A) The intermediate structures during the degradation process of the Ag₃₂ nanocluster under acidic conditions. (B) The proposed two-step transformation of the asymmetrical structural expansion from Ag₃₂ to Ag₃₃⁺-Exp.



Fig. S11[†]), the energies of the formed $\text{Ag}_{32}\text{P}_{10}\text{H}^+$ intermediates (A and B isomers) were 1.14 and 0.90 eV higher than that of the $\text{Ag}_{32}\text{P}_{10}\text{H-C}^+$ isomer, respectively. These results indicated that the H proton was more likely to attack the S site of the $\text{Ag}_3(\text{SR})_3$ ring rather than the Ag site of the $\text{Ag}(\text{PPh}_3)_2$ group at the beginning of the degradation process of Ag_{32} . Then, a large number of H protons would continuously attack the Ag site of the $\text{Ag}(\text{PPh}_3)_2$ group, gradually weakening the Ag–S bond until it broke. The DFT calculation results showed that the Ag–S bond length increased from 2.63 Å to 2.88 Å and finally to 3.06 Å under the condition of H protons continuously attacking surface Ag sites. At this time, the $\text{Ag}(\text{PPh}_3)_2$ group has completely detached from the surface of the Ag_{32} nanocluster, resulting in the formation of the Ag_{31} cluster. Similarly, the other two $\text{Ag}(\text{PPh}_3)_2$ groups would also separate from the surface of Ag_{31} with the same detaching mechanism, completing the transformation from the Ag_{32} to the Ag_{29} nanocluster.

Besides, the asymmetrical structural expansion from Ag_{32} to Ag_{33} was simulated. Due to the uneven distributions of the three terminal $\text{Ag}(\text{PPh}_3)_2$ coordination on Ag_{32} and Ag_{33} cluster surfaces, we proposed that the structural expansion from Ag_{32} to Ag_{33} followed a two-step process (Fig. 3B): (step 1) the isomerization process: the intramolecular transfer of three $\text{Ag}(\text{PPh}_3)_2$ groups on the Ag_{32} cluster surface from a uniform to a non-uniform distribution induced cluster isomerization, resulting in the formation of an Ag_{32} isomer; (step 2) the electrophilic process: the reactant $\text{Ag}(\text{PPh}_3)_1^+$ species attacked the electrophilic region of the Ag_{32} isomer and aggregated to form the Ag_{33} nanocluster. Similarly, we performed the simulation of the migration process of an $\text{Ag}(\text{PPh}_3)_2$ group on the surface as an example to reveal the isomerization transformation of the Ag_{32} nanocluster. As shown in Fig. S12,[†] the migration of an $\text{Ag}(\text{PPh}_3)_2$ group of the Ag_{32} nanocluster from site 1c to 1a was a weakly endothermic process ($\Delta E = 0.14$ eV), and the two transition-state energy barriers during the reaction were 1.29 and 0.42 eV, respectively. In the electrophilic process, the reaction sites of the Ag_{32} cluster isomer were predicted using an orbital weight dual descriptor (Δf) derived from Fukui functions.⁵³ If $\Delta f(r) > 0$, the site was favored for a nucleophilic attack. By comparison, if $\Delta f(r) < 0$, the site may be favored for an electrophilic attack. The $\text{Ag}_1(\text{PPh}_3)_1^+$ reactant received electrons and was characterized by high electrophilicity in this process. By analyzing the orbital dual descriptor of the Ag_{32} nanocluster, only three surface S sites (1b, 1c, and 3c) have negative Δf values (Fig. S13[†]), indicating that these sites could donate electrons and were susceptible to electrophilic attacks. Subsequently, we further compared the stability of the three Ag_{33} isomers. Although the Ag_{33} -1c isomer has the lowest energy, the surface $\text{Ag}_3(\text{SR})_3$ structure deformed or even collapsed, as depicted in Fig. S14.[†] The theoretical structure of the Ag_{33} -1b isomer with a lower energy was consistent with the experimental crystal structure.

Structurally, Ag_{29} and its derivative Ag_{32} or Ag_{33} nanoclusters comprised the uniform Ag_{29} framework. However, the symmetrical and asymmetrical surface structure expansions endowed the Ag_{32} and Ag_{33} nanoclusters with disparate surface

environments, which hopefully affected their supramolecular packing and physicochemical properties. The crystal lattices of these structure-correlated silver nanoclusters were compared (Fig. S15[†]). For the Ag_{29} nanocluster, the $R\text{-Ag}_{29}$ and $S\text{-Ag}_{29}$ cluster enantiomers coexisted in the crystal lattice in equal amounts, giving rise to a racemic Ag_{29} crystal (Fig. 4A and S16[†]). Of note, for a pair of Ag_{29} enantiomers (Fig. 4A), the peripheral fan-shaped Ag_4S_6 could be considered as clockwise (the orange one) and anti-clockwise (the blue one) subunits on the nanocluster surface. For differentiating the two cluster enantiomers, the clockwise-packed Ag_{29} nanocluster was referred to as $R\text{-Ag}_{29}$, while the anti-clockwise-packed one was called $S\text{-Ag}_{29}$. The terms R - and S - of other nanoclusters in this work were determined in the same way. The same racemic packing phenomenon was observed in the Ag_{32} crystal lattice (Fig. 4B and S17[†]). Consequently, although the Ag_{29} and Ag_{32} crystals presented strong PL intensities, no optical activity of the crystals was detected. In vivid contrast, the surface unsymmetric Ag_{33} nanocluster entities followed a chiral self-assembled pattern among the crystallization and the $R\text{-Ag}_{33}$ or $S\text{-Ag}_{33}$ cluster enantiomers crystallized in each crystal lattice separately (Fig. 4C, D and S18[†]), which was reminiscent of the tartaric acid. In contrast, Ag_{33} and other cluster samples exhibited quenched optical activity in the solution state (Fig. S19[†]). Accordingly, the chiral characteristic only appeared in the crystal state of the Ag_{33} nanocluster, and such nanoclusters underwent racemization during the dissolution process. In previous studies, the precise control over the transformation of nanocluster structures has been accomplished by adjusting the concentrations of ligands or metal sources, thereby allowing for the preparation of nanoclusters with specific optical activities.^{54,55} Herein, the symmetric Ag_{29} and Ag_{32} and asymmetric Ag_{33} nanoclusters formed a structure-correlated cluster series, allowing for precise correlations between cluster structures and photophysical properties.

The molecule-level and supramolecular-level asymmetric factors (*i.e.*, the unsymmetrical surface expanding and the chiral crystallography packing) exhibited great potential in rendering the Ag_{33} crystals optically active. In detail, we have collected the Ag_{33} nanocluster crystals with R - or S -crystalline packing patterns and investigated their optical activity. Specifically, all R -type (or S -type) Ag_{33} single crystals showed similar CD and CPL signals with comparable peak shapes, while the Ag_{33} single crystals with different crystalline aggregation types (*i.e.*, R - or S -type) displayed opposite CD and CPL signals, further demonstrating that the optical activity of the Ag_{33} nanocluster originated from their crystals with a “crystallization-induced spontaneous enantiomer separation” behaviour (Scheme S1[†]). As shown in Fig. 5A and B, the $R\text{-Ag}_{33}$ and $S\text{-Ag}_{33}$ crystals displayed intense signals at about 340 and 520 nm in CD spectra. Of note, the Ag_{33} crystalline film exhibits three optical absorption peaks at 350, 532, and 655 nm (Fig. 2D). The absorption peaks at 350 and 532 nm originated from the intrinsic electronic structure of the Ag_{33} molecule, which were reflected in the CD spectrum. However, the absorption peak at 655 nm of the Ag_{33} cluster crystal might arise from the distinct combinations of the electronic coupling and the lattice-origin,



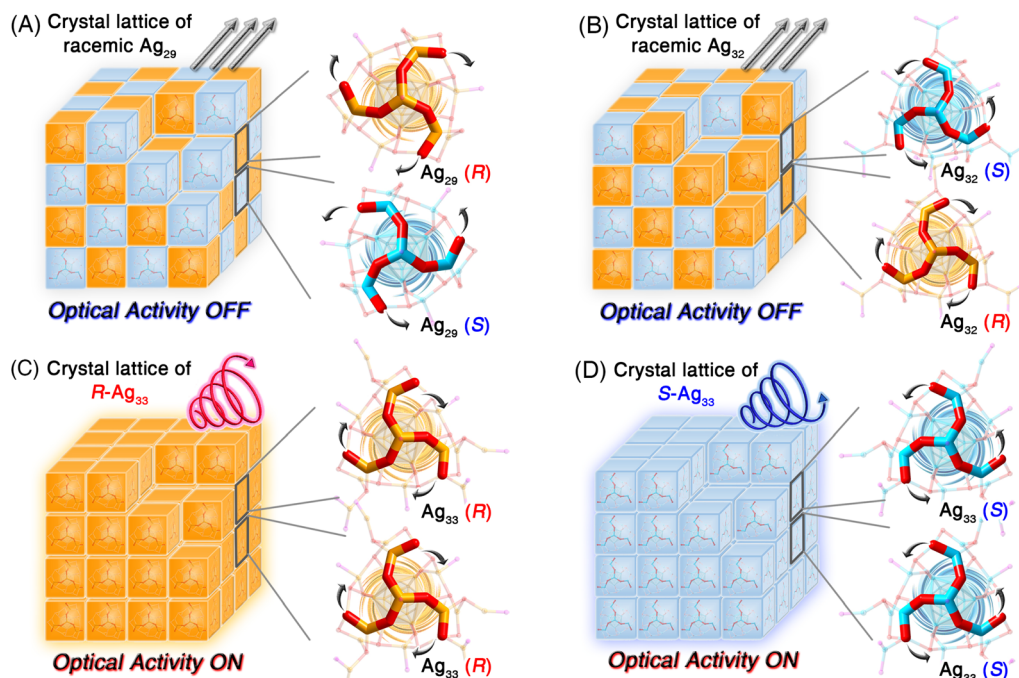


Fig. 4 Crystalline packing of Ag_{29} , Ag_{32} , and Ag_{33} nanoclusters in their crystal lattices. (A) Crystal lattice of the racemic Ag_{29} nanocluster with no optical activity. (B) Crystal lattice of the racemic Ag_{32} nanocluster with no optical activity. (C) Crystal lattice of the chiral Ag_{33} nanocluster (R enantiomer) with optical activity. (D) Crystal lattice of the chiral Ag_{33} nanocluster (S enantiomer) with optical activity.

non-radiative decay pathways occurring through electron-phonon interactions, which might be the possible reason why the 655 nm signal was not reflected in the CD spectrum.

Besides, the CPL spectra of $R\text{-Ag}_{33}$ and $S\text{-Ag}_{33}$ crystals showed mirror signals at about 760 nm, demonstrating the apparent optical activity of the Ag_{33} crystals (Fig. 5C and D). In addition,

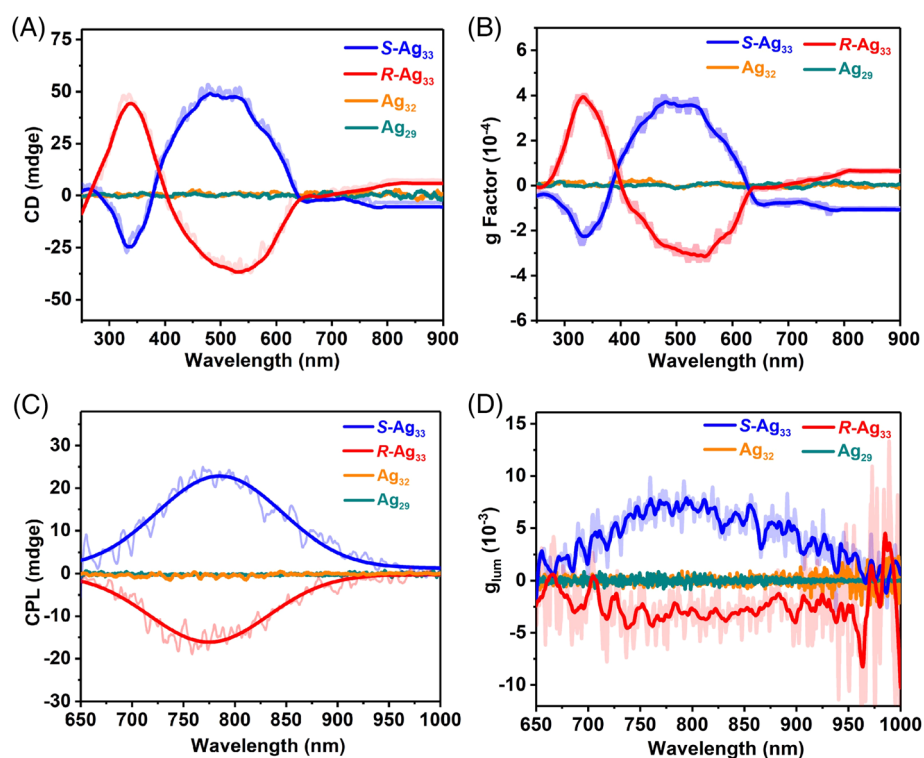


Fig. 5 Optical activity test of cluster crystals. (A) Circular dichroism spectra of the four nanoclusters in the crystal state. (B) g factors of the CD results of different cluster crystals. (C) Circularly polarized luminescence spectra of the four nanoclusters in the crystal state. (D) g_{lum} of the CPL results of different cluster crystals.



the crystals of Ag₃₃ nanoclusters showed consistent optical activity by analyzing the CPL results of different points/sides of the crystals or microcrystals (Fig. S20†), demonstrating that the optical activity originated from the nanocluster crystals themselves, *i.e.*, the chiral crystalline packing of the Ag₃₃ nanoclusters in the crystal lattice. In contrast, the Ag₂₉-BDT, Ag₂₉, and Ag₃₂ crystals were optically inactive with no signals in CD and CPL characterization.

Conclusion

In summary, the continuous size growth of metal nanoclusters has been accomplished within a preserved framework, including symmetrical surface structure expansion from Ag₂₉ to Ag₃₂ and asymmetrical expansion from Ag₃₂ to Ag₃₃, allowing for nanocluster growth to be meticulously dictated with atomic precision. The symmetrical degradation and the asymmetrical expansion for transforming the geometric structures of nanoclusters were rationalized *via ab initio* calculations. Besides, the structure-dependent optical properties, including absorption and emission characteristics, of these correlated silver nanoclusters were investigated. More importantly, the molecule-level and supramolecular-level asymmetric factors (*i.e.*, the unsymmetrical surface expanding and the chiral crystallography packing) of the Ag₃₃ nanocluster rendered its crystals highly optically active, derived from CD and CPL characterization. This work presented an important structure-correlated cluster series with controllable symmetrical/asymmetrical surface environments, allowing for some new insights into the cluster structure evolutions.

Data availability

The data that support the findings of this study are available in the ESI† of this article.

Author contributions

H. Shen conceived and carried out experiments. P. Wang performed the theoretical simulation. J. Xu and Z. Fu assisted in the synthesis and optical spectral measurements. X. Kang analyzed the data and wrote the paper and Y. Pei and M. Zhu supervised the project. All authors commented on and agreed on the manuscript.

Conflicts of interest

The authors declare no competing financial interests.

Acknowledgements

We acknowledge the financial support of the NSFC (22371003, 22101001, and 22471001), the Ministry of Education, the Natural Science Foundation of Anhui Province (2408085Y006), the University Synergy Innovation Program of Anhui Province (GXXT-2020-053), and the Scientific Research Program of Universities in Anhui Province (2022AH030009). Y. P.

acknowledges financial support from the NSFC (22373082). P. W. acknowledges financial support from the Scientific Research Fund of Hunan Provincial Education Department (22B0154).

Notes and references

- 1 Y. Xia, Y. Xiong, B. Lim and S. E. Skrabalak, *Angew. Chem., Int. Ed.*, 2009, **48**, 60–103.
- 2 M. R. Jones, K. D. Osberg, R. J. Macfarlane, M. R. Langille and C. A. Mirkin, *Chem. Rev.*, 2011, **111**, 3736–3827.
- 3 Q. N. Nguyen, C. Wang, Y. Shang, A. Janssen and Y. Xia, *Chem. Rev.*, 2023, **123**, 3693–3760.
- 4 M. J. Walsh, W. Tong, H. Katz-Boon, P. Mulvaney, J. Etheridge and A. M. Funston, *Acc. Chem. Res.*, 2017, **50**, 2925–2935.
- 5 S. E. Skrabalak, *Acc. Mater. Res.*, 2021, **2**, 621–629.
- 6 Y. Xia, X. Xia and H.-C. Peng, *J. Am. Chem. Soc.*, 2015, **137**, 7947–7966.
- 7 C. J. DeSantis and S. E. Skrabalak, *J. Am. Chem. Soc.*, 2013, **135**, 10–13.
- 8 J. D. Smith, E. Bladt, J. A. C. Burkhart, N. Winckelmans, K. M. Koczur, H. M. Ashberry, S. Bals and S. E. Skrabalak, *Angew. Chem., Int. Ed.*, 2020, **59**, 943–950.
- 9 R. Jin, C. Zeng, M. Zhou and Y. Chen, *Chem. Rev.*, 2016, **116**, 10346–10413.
- 10 I. Chakraborty and T. Pradeep, *Chem. Rev.*, 2017, **117**, 8208–8271.
- 11 M. F. Matus and H. Häkkinen, *Nat. Rev. Mater.*, 2023, **8**, 372–389.
- 12 S. Kenzler and A. Schnepf, *Chem. Sci.*, 2021, **12**, 3116–3129.
- 13 W. Jing, H. Shen, R. Qin, Q. Wu, K. Liu and N. Zheng, *Chem. Rev.*, 2023, **123**, 5948–6002.
- 14 Z. Wang, Y.-J. Zhu, Y.-Z. Li, G.-L. Zhuang, K.-P. Song, Z.-Y. Gao, J.-M. Dou, M. Kurmoo, C.-H. Tung and D. Sun, *Nat. Commun.*, 2022, **13**, 1802.
- 15 E. L. Albright, T. I. Levchenko, V. K. Kulkarni, A. I. Sullivan, J. F. DeJesus, S. Malola, S. Takano, M. Nambo, K. Stamplecoskie, H. Häkkinen, T. Tsukuda and C. M. Crudden, *J. Am. Chem. Soc.*, 2024, **146**, 5759–5780.
- 16 R.-W. Huang, X. Song, S. Chen, J. Yin, P. Maity, J. Wang, B. Shao, H. Zhu, C. Dong, P. Yuan, T. Ahmad, O. F. Mohammed and O. M. Bakr, *J. Am. Chem. Soc.*, 2023, **145**, 13816–13827.
- 17 L. Fang, W. Fan, G. Bian, R. Wang, Q. You, W. Gu, N. Xia, L. Liao, J. Li, H. Deng, N. Yan and Z. Wu, *Angew. Chem., Int. Ed.*, 2023, **62**, e202305604.
- 18 S.-S. Zhang, S. Havenridge, C. Zhang, Z. Wang, L. Feng, Z.-Y. Gao, C. M. Aikens, C.-H. Tung and D. Sun, *J. Am. Chem. Soc.*, 2022, **144**, 18305–18314.
- 19 Z. Wang, Y. Wang, C. Zhang, Y.-J. Zhu, K.-P. Song, C. M. Aikens, C.-H. Tung and D. Sun, *Natl. Sci. Rev.*, 2024, **11**, nwa192.
- 20 S.-S. Zhang, R.-C. Liu, X.-C. Zhang, L. Feng, Q.-W. Xue, Z.-Y. Gao, C.-H. Tung and D. Sun, *Sci. China:Chem.*, 2021, **64**, 2118–2124.



- 21 R.-W. Huang, Y.-S. Wei, X.-Y. Dong, X.-H. Wu, C.-X. Du, S.-Q. Zang and T. C. W. Mak, *Nat. Chem.*, 2017, **9**, 689–697.
- 22 X. Zhang and H. Xu, *Angew. Chem., Int. Ed.*, 2024, **63**, e202317597.
- 23 C. A. Hosier and C. J. Ackerson, *J. Am. Chem. Soc.*, 2018, **141**, 309–314.
- 24 J. Zhao, A. Ziarati, A. Rosspeintner and T. Bürgi, *Angew. Chem., Int. Ed.*, 2024, **63**, e202316649.
- 25 L.-J. Liu, F. Alkan, S. Zhuang, D. Liu, T. Nawaz, J. Guo, X. Luo and J. He, *Nat. Commun.*, 2023, **14**, 2397.
- 26 K.-Y. Huang, Z.-Q. Yang, M.-R. Yang, T.-S. Chen, S. Tang, W.-M. Sun, Q. Yao, H.-H. Deng, W. Chen and J. Xie, *J. Am. Chem. Soc.*, 2024, **146**, 8706–8715.
- 27 C.-Y. Liu, S.-F. Yuan, S. Wang, Z.-J. Guan, D.-e. Jiang and Q.-M. Wang, *Nat. Commun.*, 2022, **13**, 2082.
- 28 Y. Horita, S. Hossain, M. Ishimi, P. Zhao, M. Sera, T. Kawawaki, S. Takano, Y. Niihori, T. Nakamura, T. Tsukuda, M. Ehara and Y. Negishi, *J. Am. Chem. Soc.*, 2023, **145**, 23533–23540.
- 29 A. Baksi, E. K. Schneider, P. Weis, I. Chakraborty, O. Fuhr, S. Lebedkin, W. J. Parak and M. M. Kappes, *ACS Nano*, 2020, **14**, 15064–15070.
- 30 G. Soldan, M. A. Aljuhani, M. S. Bootharaju, L. G. AbdulHalim, M. R. Parida, A.-H. Emwas, O. F. Mohammed and O. M. Bakr, *Angew. Chem., Int. Ed.*, 2016, **55**, 5749–5753.
- 31 Y. Zeng, S. Havenridge, M. Gharib, A. Baksi, K. L. D. M. Weerawardene, A. R. Ziefuß, C. Strelow, C. Rehbock, A. Mews, S. Barcikowski, M. M. Kappes, W. J. Parak, C. M. Aikens and I. Chakraborty, *J. Am. Chem. Soc.*, 2021, **143**, 9405–9414.
- 32 H. Seong, Y. Jo, V. Efremov, Y. Kim, S. Park, S. M. Han, K. Chang, J. Park, W. Choi, W. Kim, C. H. Choi, J. S. Yoo and D. Lee, *J. Am. Chem. Soc.*, 2023, **145**, 2152–2160.
- 33 A. Chakraborty, A. C. Fernandez, A. Som, B. Mondal, G. Natarajan, G. Paramasivam, T. Lahtinen, H. Häkkinen and T. Pradeep, *Angew. Chem., Int. Ed.*, 2018, **57**, 6522–6526.
- 34 X. Wang, J. Zhao, H. Eliasson, R. Erni, A. S. McKeown Walker and T. Bürgi, *J. Am. Chem. Soc.*, 2023, **145**, 27273–27281.
- 35 R.-Q. Chen, S.-T. Wang, Y.-J. Liu, J. Zhang and W.-H. Fang, *J. Am. Chem. Soc.*, 2024, **146**, 7524–7532.
- 36 Q. You, H. Wang, Y. Zhao, W. Fan, W. Gu, H.-L. Jiang and Z. Wu, *J. Am. Chem. Soc.*, 2024, **146**, 9026–9035.
- 37 C. Zeng, Y. Chen, K. Iida, K. Nobusada, K. Kirschbaum, K. J. Lambright and R. Jin, *J. Am. Chem. Soc.*, 2016, **138**, 3950–3953.
- 38 X. Zou, X. Kang and M. Zhu, *Chem. Soc. Rev.*, 2023, **52**, 5892–5967.
- 39 W. Ishii, Y. Okayasu, Y. Kobayashi, R. Tanaka, S. Katao, Y. Nishikawa, T. Kawai and T. Nakashima, *J. Am. Chem. Soc.*, 2023, **145**, 11236–11244.
- 40 Z. Luo, V. Nachammai, B. Zhang, N. Yan, D. T. Leong, D.-e. Jiang and J. Xie, *J. Am. Chem. Soc.*, 2014, **136**, 10577–10580.
- 41 W. W. Xu, Y. Li, Y. Gao and X. C. Zeng, *Nanoscale*, 2016, **8**, 7396–7401.
- 42 M. S. Bootharaju, C. P. Joshi, M. J. Alhilaly and O. M. Bakr, *Chem. Mater.*, 2016, **28**, 3292–3297.
- 43 X. Wei, H. Li, Z. Zuo, F. Song, X. Kang and M. Zhu, *J. Am. Chem. Soc.*, 2023, **145**, 13750–13757.
- 44 L. G. AbdulHalim, Z. Hooshmand, M. R. Parida, S. M. Aly, D. Le, X. Zhang, T. S. Rahman, M. Pelton, Y. Losovyj, P. A. Dowben, O. M. Bakr, O. F. Mohammed and K. Katsiev, *Inorg. Chem.*, 2016, **55**, 11522–11528.
- 45 M. Waszkielewicz, J. Olesiak-Banska, C. Comby-Zerbino, F. Bertorelle, X. Dagany, A. K. Bansal, M. T. Sajjad, I. D. W. Samuel, Z. Sanader, M. Rozycka, M. Wojtas, K. Matczyszyn, V. Bonacic-Koutecky, R. Antoine, A. Ozyhard and M. Samoc, *Nanoscale*, 2018, 11335–11341.
- 46 H. Shen, J. Xu, Z. Fu, X. Wei, X. Kang, W. Shi and M. Zhu, *Angew. Chem., Int. Ed.*, 2024, **63**, e202317995.
- 47 L. G. AbdulHalim, M. S. Bootharaju, Q. Tang, S. Del Gobbo, R. G. AbdulHalim, M. Eddaoudi, D.-e. Jiang and O. M. Bakr, *J. Am. Chem. Soc.*, 2015, **137**, 11970–11975.
- 48 M. Walter, J. Akola, O. Lopez-Acevedo, P. D. Jadzinsky, G. Calero, C. J. Ackerson, R. L. Whetten, H. Grönbeck and H. Häkkinen, *Angew. Chem., Int. Ed.*, 2008, **105**, 9157–9162.
- 49 X.-Y. Dong, H.-L. Huang, J.-Y. Wang, H.-Y. Li and S.-Q. Zang, *Chem. Mater.*, 2018, **30**, 2160–2167.
- 50 H. Döllefeld, H. Weller, A. Eychmüller and J. Phy, *Chem. B.*, 2002, **106**, 5604–5608.
- 51 J. Zhang, C. Rowland, Y. Liu, H. Xiong, S. Kwon, E. Shevchenko, R. D. Schaller, V. B. Prakapenka, S. Tkachev and T. Rajh, *J. Am. Chem. Soc.*, 2015, **137**, 742–749.
- 52 X. Wei, X. Kang, Z. Zuo, F. Song, S. Wang and M. Zhu, *Nat. Sci. Rev.*, 2021, **8**, nwa077.
- 53 R. Pino-Rios, O. Yañez, D. Inostroza, L. Ruiz, C. Cardenas, P. Fuentealba and W. Tiznado, *Angew. Chem., Int. Ed.*, 2017, **38**, 481–488.
- 54 C. Zhang, W.-D. Si, Z. Wang, C.-H. Tung and D. Sun, *Angew. Chem., Int. Ed.*, 2024, **63**, e202404545.
- 55 X.-L. Peng, S. Huang, Y.-J. Zhao, X.-M. Luo, H.-Y. Li, J.-H. Hu, J.-H. Huang and S.-Q. Zang, *Sci. Bull.*, 2024, DOI: [10.1016/j.scib.2024.09.047](https://doi.org/10.1016/j.scib.2024.09.047).

